nature materials

Article

https://doi.org/10.1038/s41563-026-02680-w

Hydrogen-induced damage in Ni-based superalloys at elevated temperatures

Received: 20 November 2025

Accepted: 22 June 2026

Published online: 27 July 2026

Check for updates

Shuai Kong[1,6], Xizhen Dong[2,6], Zheng Zhong[3,6], Jie Hou[3], Yubo Zhao[1], Baptiste Gault[2,4], Shaolou Wei[2], Aparna Saksena[2], Kai-Shang Li[1,5], Binhan Sun[1,5] ✉, Xian-Cheng Zhang[1,5] ✉, Dierk Raabe[2] ✉ & Shan-Tung Tu[1]

The urgent need to decarbonize the energy and transport sectors motivates the use of hydrogen-containing fuels in gas turbines for power generation and aviation applications, exposing safety-critical components to hydrogen environments at elevated temperatures. Ambient-temperature hydrogen embrittlement has long been interpreted through the physical interactions between hydrogen and microstructural defects like interfaces and dislocations. Here we show that this understanding does not fully capture the behaviour at elevated temperatures, where vacancy-driven chemical reactions between hydrogen and specific microstructural constituents can markedly intensify embrittlement compared with ambient conditions. In a prototypical face-centred cubic Ni-based superalloy, our near-atomic-scale characterization and ab initio calculations reveal strong trapping of hydrogen atoms in carbon vacancies in carbides, driving their partial decomposition while simultaneously triggering localized methane formation at the carbide–matrix interface. As a result, the heterointerfaces are weakened, rendering them vulnerable to deformation-induced damage. Our work provides a physical foundation for mechanistic modelling of elevated-temperature hydrogen embrittlement in Ni-based alloys, an emerging area critical to hydrogen-fuelled turbines and related high-temperature technologies.

Unprecedented demand for hydrogen (H) as a versatile energy carrier is now propelling its expansion into broader domains such as H_2-fuelled gas turbines and aerospace engines[1,2]. Given that gas turbines account for approximately 22% of global electricity generation (~31,153 TWh year^{-1}) and contribute around 15% of global CO_2 emissions (~37,566 Mt year^{-1}), the transition from fossil to H-based fuels in gas turbines represents one of the most impactful strategies for mitigating global warming[3]. Recent developments in commercial aviation also suggest promising prospects for using H directly as a fuel in jet turbines, a technology that demands the utmost safety[4]. Materials constituting the structural components of these engineering devices are increasingly exposed to extreme operation temperatures and H-rich atmospheres[5]. Such harsh coupled environmental conditions notably elevate the risk of material degradation[6], challenging the longevity and reliability of entire components, thus questioning an essential pillar of future CO_2-free energy supply and clean air traffic. The key

[1]Key Laboratory of Pressure Systems and Safety, Ministry of Education, East China University of Science and Technology, Shanghai, China. [2]Max Planck Institute for Sustainable Materials, Düsseldorf, Germany. [3]College of Materials Science and Engineering, State Key Laboratory of Cemented Carbide, Hunan University, Changsha, China. [4]Groupe de Physique des Matériaux, UMR 6634, Université de Rouen Normandie, CNRS, INSA Rouen Normandie, Rouen, France. [5]State Key Laboratory of Chemical Safety, East China University of Science and Technology, Shanghai, China. [6]These authors contributed equally: Shuai Kong, Xizhen Dong, Zheng Zhong. ✉e-mail: binhan.sun@ecust.edu.cn; xczhang@ecust.edu.cn; d.raabe@mpi-susmat.de

https://doi.org/10.1038/s41563-026-02680-w

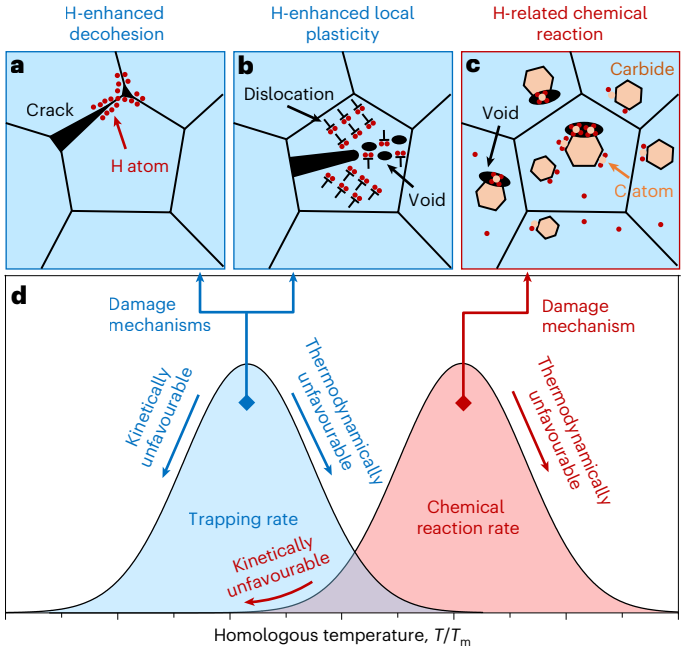

Fig. 1 | The influence of temperature on H-associated interactions and reactions with microstructural constituents and the resulting prevalent H-embrittlement mechanisms. a, Damage formation due to H-enhanced interface decohesion. **b**, Interaction between H and dislocations, which alters the local mechanical response and induces plastic instability, promoting damage formation. **c**, H-related chemical reaction with carbides. **d**, Schematic illustration of the temperature-dependent H-induced damage mechanisms. The blue-shaded region denotes the H trapping rate, which is defined as the number of H atoms being captured by microstructural trapping sites per unit time. At low temperatures, H trapping is kinetically hindered by limited diffusivity, whereas at elevated temperatures, thermal activation promotes detrapping, rendering trapping thermodynamically unfavourable. A characteristic rise-then-fall trend with increasing temperature is thus proposed, as also described by the McNabb–Foster model[14]. The red-shaded region represents the chemical reaction rate between H and C-containing microstructural constituents, defined as the change in the reaction product (for example, CH_4) per unit of time. The reaction activation barrier is difficult to overcome at low temperatures due to limited atom diffusion (kinetically unfavourable), and the reaction becomes thermodynamically unfavourable at elevated temperatures because of the decomposition of certain reaction products[38]. The apparent reaction rate thus often peaks at an intermediate temperature[39]. Both the H-trapping rate and H-related reaction rate are plotted as a function of the homologous temperature (temperature divided by melting temperature, T/T_m).

challenge lies in understanding and counteracting H-induced damage, also referred to as H embrittlement, causing abrupt, complete loss of a material's load-bearing capacity in H-containing environments[7–9].

The current understanding of the underlying H-accelerated damage nucleation and evolution mechanisms involves the complex interactions between solute H atoms and microstructural defects such as dislocations and interfaces[7,9]. At near-ambient temperatures, H atoms tend to segregate to or become trapped at various types of defects (for example, interfaces and dislocations)[10–12], influencing their properties and thus promoting the formation of damage upon loading[7,9] (Fig. 1a,b). However, these effects are essentially weakened at elevated temperatures because of the thermal-activation-enhanced H detrapping from microstructural trapping sites[12–14] and thus the reduced rate of H trapping (Fig. 1d). In carbon steels, H can react with solute carbon (C) atoms at sufficiently high temperatures, resulting in the formation of internal cavities associated with methane formation[15–18]. However, such a mechanism is less likely to operate in alloy systems lacking a notable amount of solute C, such as Ni-based superalloys[16,18]. In fact, H embrittlement in these alloys has often been less of a concern at higher temperatures[19], although limited data suggest that it can still occur under specific conditions[20]. Yet the underlying damage mechanisms at elevated temperatures in Ni-based superalloys remain unclear, which hampers their design and the assurance of structural integrity in components used in H_2-powered gas turbines and aviation systems.

Here we show that the IN718 alloy, the prototypical forged Ni-based superalloy—the most widely used material for high-temperature power-conversion applications—can be strongly damaged by H when mechanically loaded in situ under a few megapascals of H_2 pressure at elevated temperatures (for example, 400 °C). We elucidate the role of H in modifying the thermodynamic and kinetic characteristics of various microstructural defects and the corresponding transition in embrittlement mechanisms in response to increased temperatures (as schematically shown in Fig. 1d). We find that at sufficiently high temperatures, where the H trapping of certain types of defects (dislocations and interfaces) diminishes, direct chemical reactions between H and microstructural constituents (here, MC carbide) become thermodynamically and kinetically favourable (Fig. 1c). Such reactions promote a carbide transition into M_6C_5-type or M_2C-type phases that are C depleted, a state that catalyses localized methane formation at the carbide–matrix interface, accelerating its decohesion when exposed to external stresses. This vacancy-driven selective dealloying mechanism, elucidated in this study, fundamentally differs from ambient-temperature H-related embrittlement mechanisms, thereby advancing the current understanding of H-induced damage and H embrittlement in Ni-based alloys.

H-induced degradation of properties at elevated temperatures

The microstructure of the alloy after solid-solution treatment and standard two-step ageing (Methods) is a face-centred cubic (fcc) γ-matrix with an average grain size of approximately 19.8 μm (Fig. 2a). The ageing process leads to precipitation of two strengthening phases, identified as γ′ with a fcc ($L1_2$) structure and γ″ with a body-centred tetragonal (DO_{22}) structure[21,22] (Fig. 2b). The formation of the δ phase, with an orthorhombic (DO_a) structure, is also observed at grain boundaries and in the grain interior[21,23] (Fig. 2a and Extended Data Fig. 1). Additionally, primary MC carbides, enriched in Nb and Ti, are also present (Fig. 2a–c). These carbides, which under H-free conditions are thermodynamically stable and form already during solidification, are crucial in controlling the mechanical behaviour of the studied material and similar Ni-based alloys, due to their role in refining the grain size as well as in suppressing grain-boundary sliding upon mechanical loading at high temperatures[21,24]. Transmission electron microscopy (TEM) analysis, shown in Fig. 2b, reveals that these (Nb,Ti)C carbides possess an fcc (B1) structure with a lattice constant of 4.43 Å. Notably, from atom probe tomography (APT) analysis, the C concentration in the carbide is 41.2 at.% (Fig. 2c and Supplementary Fig. 1a). Quantifying C by APT is challenging (Methods), but this concentration is well below what has previously been reported as possible losses in a range of carbides[25,26], and thus this result is a clear indication of a non-stoichiometric carbide, that is, including structural vacancies within the non-metallic sublattice[27]. These vacancies, formed through high-temperature self-diffusion, allow the composition of the carbides to vary, thereby causing a substantially drop in C concentration, without changing their crystal structure[27].

When the alloy with the aforementioned representative microstructure was exposed to 2 MPa gaseous H_2 under simultaneous (or in situ) tensile loading at 400 °C, a clear reduction in total elongation (by 14.9% in comparison to a reference sample loaded under Ar) was observed, as shown in Fig. 2d. The corresponding reduction in cross-sectional area (another critical indication of a material's ductility) is decreased by ~18.8% due to the presence of H at this temperature (inset in Extended Data Fig. 2c). This level of H-induced ductility loss is approximately twice that at room temperature (8.9% of total elongation

https://doi.org/10.1038/s41563-026-02680-w

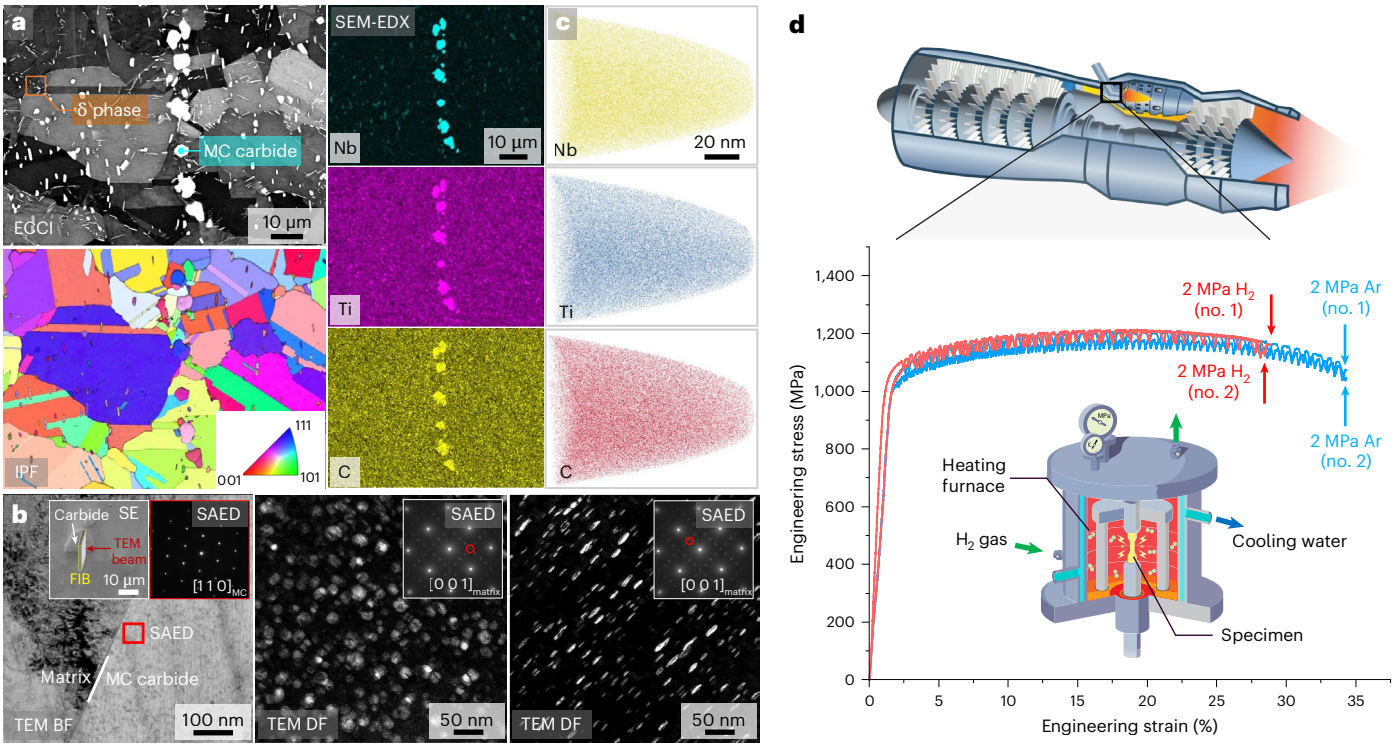

Fig. 2 | Microstructure of the studied material (IN718 alloy), commonly used in gas turbines or jet engines, and the influence of H_2 atmosphere on the tensile properties at 400 °C. a, Electron channelling contrast imaging (ECCI), the electron backscatter diffraction (EBSD) inverse pole figure (IPF) and the corresponding scanning electron microscopy (SEM)-based energy-dispersive X-ray spectroscopy (EDX) maps showing the fcc γ-matrix with embedded MC carbides and δ phase. **b**, TEM bright-field (BF) image of MC carbide (left) and dark-field (DF) images of the γ′ and γ″ phases (centre and right, respectively). The selected area electron diffraction (SAED) patterns, shown as insets, reveal the crystal structure of the MC carbide and the crystallographic orientation relationships between the γ-matrix and the γ′ and γ″ phases. A secondary-electron (SE) image is inset into the left image to indicate the location where FIB milling was performed. The small red circles in the SAED panels indicate the characteristic diffraction spots used for phase identification. **c**, APT atomic mapping of Nb, Ti and C atoms of a MC carbide. The overall C concentration was determined to be ~41.2 at.%. **d**, Schematic diagram of a gas turbine or jet engine (top) and H-embrittlement response of the IN718 alloy used in such applications (bottom). Tensile stress–strain curves of the material mechanically loaded under 2 MPa H_2 and Ar at 400 °C at the strain rate of ~2.9×10^{-5} s^{-1} are shown. The curve obtained in the Ar atmosphere serves as a reference to reveal the occurrence of H-induced damage and its degradation effect on the material's property. For each condition, at least three tests were conducted (two representative curves are shown here), yielding standard deviations (s.d.) of total elongation of 0.45% in Ar and 1.10% in H_2. The inset schematic diagram displays the custom-designed high-temperature in situ H-charging and tensile-testing apparatus.

reduction and 9.4% of reduction in cross-sectional area under the same H_2 pressure; Extended Data Fig. 2a), a temperature regime widely considered to exert the most severe H-embrittlement effect on Ni-based alloys and similar fcc materials[9,20]. When the strain rate is reduced from ~2.9×10^{-5} s^{-1} to ~1.3×10^{-5} s^{-1} (Extended Data Fig. 3a,b), or when the specimens are pre-charged with H prior to testing (Extended Data Fig. 3c,d), the resulting increase in H uptake leads to a markedly more severe H-induced ductility loss (up to 29.4% reduction of total elongation, as shown in Extended Data Fig. 3b). At the testing temperature of 400 °C, a serrated plastic flow phenomenon known as the Portevin–Le Chatelier effect is observed. Its occurrence has been demonstrated to stem from the dynamic interaction between mobile dislocations and diffusing solute atoms[28]. The presence of H does not appear to noticeably influence this effect, as the average stress-drop amplitude is very similar for the two scenarios (29.2 ± 7.1 MPa under Ar and 33.9 ± 7.8 MPa under H_2).

Characterization of H-induced damage at elevated temperatures

Unlike the H-induced fracture behaviour at lower temperatures (for example, 25 °C and 200 °C, corresponding to the lower temperature regime as indicated in Fig. 1d), which is dominated by H-promoted interface decohesion and intermetallic cracking, both associated with the δ phase[29] (Extended Data Fig. 4), we did not detect any such intergranular or cleavage-type fracture features at 400 °C under H_2 atmosphere. Instead, the fracture surface at this temperature was mainly characterized by well-defined dimples embedded with cracked carbides (Fig. 3a). Statistical analysis of H-induced damage across a large area (~500 × 2,000 μm²) reveals two prevalent cracking modes associated with MC carbides: carbide–matrix interfacial decohesion and internal cracking of carbides. We then performed a systematic comparison of the damage sites and quantified the origin of the damage under four distinct conditions: (1) the initial state devoid of any charging or deformation; (2) the sample exposed to 2 MPa H_2 at 400 °C for ~0.5 h (equivalent to the time spent for the tensile testing) without mechanical loading; and the tensile fractured sample tested at elevated temperature under (3) H_2 or (4) Ar. The results are summarized in Fig. 3b.

The proportion of carbide–matrix interfacial decohesion is shown to be already markedly increased by a factor of ~4.9 through H charging alone at 400 °C (conditions (1) and (2)). One representative example of such interface cracking is highlighted in Fig. 3c. The increased point-to-point crystallographic misorientation angle close to the interface crack indicates a high strain concentration in these regions. Given that no external loading had been applied, this localized deformation arises from H charging and the resulting damage nucleation, the associated volume expansion of which imposes additional compressive stress on the neighbouring matrix. The clear absence of such strain concentration close to the carbide interface in the initial, non-charged microstructure (Supplementary Fig. 2) further supports this point.

https://doi.org/10.1038/s41563-026-02680-w

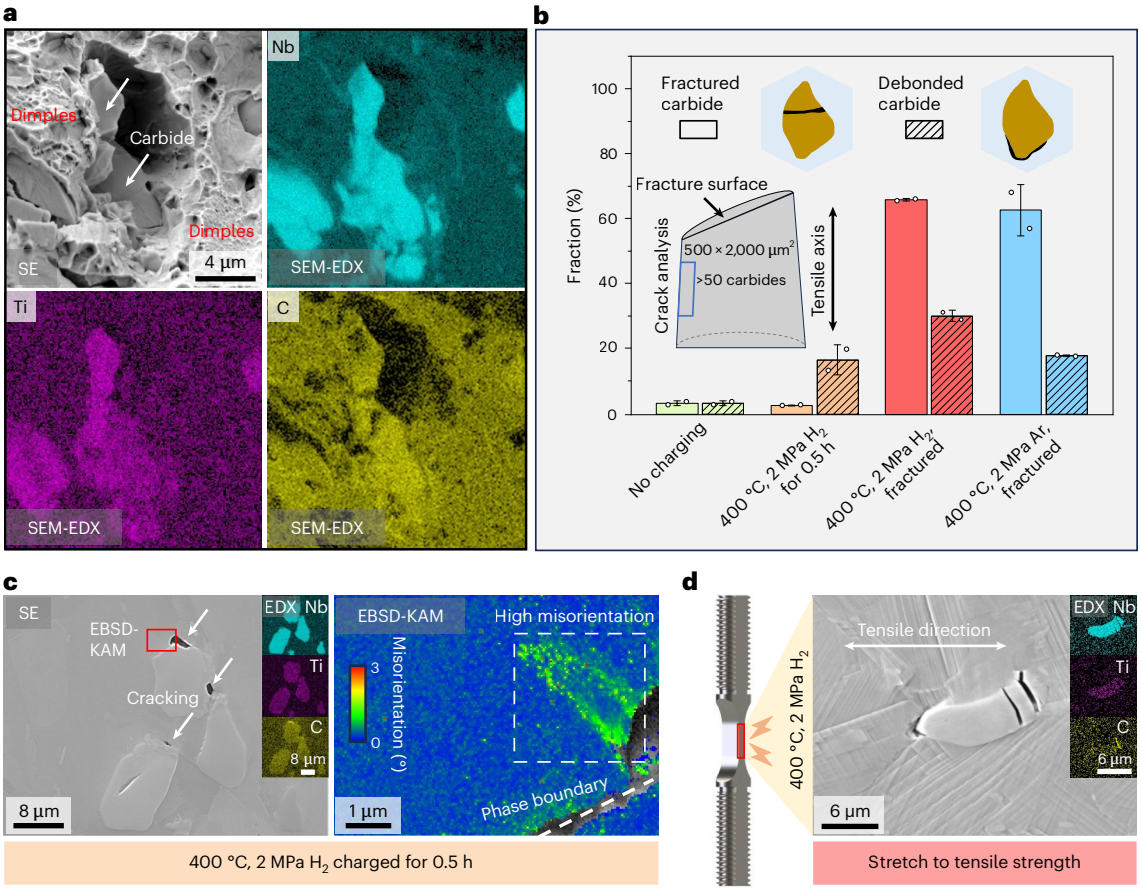

Fig. 3 | H-induced damage behaviour at 400 °C. a, Representative SE image and the corresponding SEM-EDX mapping of the fracture surface of the sample that failed in an H atmosphere. **b**, Statistical analysis of micro-cracks in a longitudinal section of samples under different charging and mechanical-loading scenarios. A large area of 500 × 2,000 μm² close to the sample surface within the H penetrating depth (~1,500 μm; Extended Data Fig. 7) was probed (left inset). More than 50 carbides for each sample were analysed. The top inset schematic diagrams illustrate two modes of carbide cracking: internal fracture (top left) and carbide–matrix interfacial decohesion (top right). Data are presented as mean values ± s.d. Individual white dots represent independent samples ($n = 2$ for each condition). **c**, SE image and the inset SEM-EDX mapping showing a typical example of carbide–matrix interfacial debonding after 0.5 h charging under 2 MPa H_2 exposure at 400 °C. The corresponding EBSD kernel average misorientation (KAM) map on the right reveals localized plastic deformation in the γ-matrix adjacent to the crack (marked by the red box). **d**, The H-induced cracking in the tensile sample that is stretched to its tensile strength under 2 MPa H_2 at 400 °C. The corresponding SEM-EDX mapping inset in this image confirms the fractured carbide at this location.

Upon simultaneous mechanical loading and H charging, both carbide cracking and debonding events occur more frequently, as shown in Fig. 3b,d. Yet the fraction of the latter damage mode is much higher under H_2 atmosphere (30.3%) than under Ar (18.1%) when applying the same mechanical testing parameters. These results suggest that the primary damaging effect of H at elevated temperatures lies in its promotion of decohesion or debonding between MC carbides and the matrix, mechanisms that serve as principal causes of sample failure.

H trapping and carbide phase transition near damage sites

To further investigate carbide-associated damage mechanisms, we conducted a detailed characterization of microstructural changes and hydrogen trapping, with a particular focus on regions adjacent to the cracked carbide–matrix interface (Fig. 4a–c and Extended Data Fig. 5). At these locations, we observe a clear superlattice diffraction pattern of the carbide (Fig. 4c), which is in sharp contrast to the structure observed within the carbide interior, which maintains its initial fcc (B1) structure without much change in lattice parameter (4.40 Å; Fig. 4b). These superlattice spots correspond well to the vacancy-ordered M_6C_5-type carbide ($C2/m$ space group)[27,30]. Crucially, this superlattice structure had been observed neither in the initial microstructure (Fig. 2b) nor in the sample deformed under the 400 °C Ar reference test condition (Extended Data Fig. 6). We thus conclude that the observed structural carbide decomposition, that is, its transition into a C-depleted state, reflected by the formation of a different superlattice structure, is a direct consequence of the carbide's chemical reaction with H at this temperature. Such a phase transition is likely to occur close to the carbide–matrix interface, the region where H ingress from the matrix begins and which thus should be most enriched with H.

We then employed APT to analyse the elemental information near the carbide–matrix interface. Site-specific APT specimen preparation was performed, targeting an interface that had been partially cracked under simultaneous H_2 exposure and mechanical loading (Fig. 4d). The subsequent sharpening process was carried out at a cryogenic temperature of −190 °C, with the stage precooled by liquid nitrogen (Fig. 4e), aiming to limit H uptake during the focused ion beam (FIB) milling process[31,32]. Figure 4f displays the atomic maps, and the H distribution is also highlighted in the corresponding two-dimensional contour map. The results reveal a pronounced H enrichment in the carbide region within a few nanometres of the carbide–matrix interface. This enrichment reaches up to ~13 at.% near the heterointerface, in contrast to ~4 at.% in the carbide interior and ~2 at.% in the fcc matrix, as quantified by the one-dimensional concentration profile across the interface (Fig. 4g). Details of the methodology to assess the validity of the H assessment are provided in the Methods. Because of the small

https://doi.org/10.1038/s41563-026-02680-w

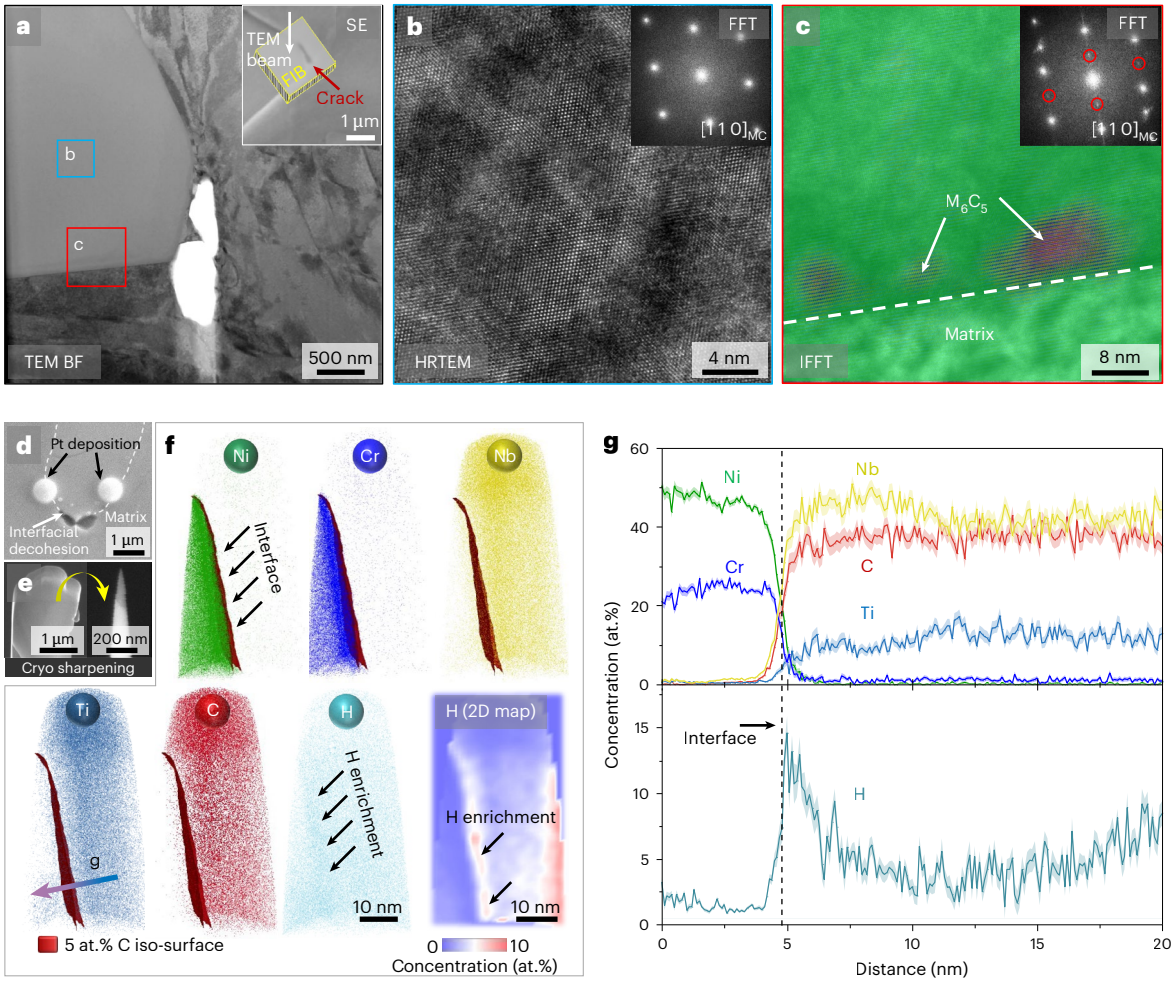

Fig. 4 | Microstructure analysis of regions close to carbide–matrix interfaces that are damaged upon H_2 exposure and simultaneous mechanical loading at 400 °C. a, The overview bright-field TEM image of a cracked carbide–matrix interface, with a SE inset showing the corresponding FIB-lifted area. **b**, High-resolution TEM (HRTEM) image taken from the blue box marked in **a** and the corresponding fast Fourier transformation (FFT) image, showing the lattice structure of the carbide interior. **c**, Inverse FFT (IFFT) image based on the superlattice reflection spots marked in the inset FFT image, suggesting the formation of vacancy-ordered M_6C_5-type carbide ($C2/m$ space group). **d**, SE image of another cracked carbide–matrix interface in the same sample, showing the location where APT samples were taken. **e**, APT sample preparation using FIB milling at the cryogenic temperature. **f**, APT analysis including atomic maps of individual elements (Ni, Cr, Nb, Ti, C and H) and a two-dimensional (2D) contour map of H, showing the enrichment of H close to the carbide–matrix interface. The iso-surface (5 at.% C) was used to delineate the position of the phase boundary. **g**, One-dimensional composition profiles across the heterointerface within a 15 nm diameter cylindrical region along the arrow marked in **f**. The shaded bands of the traces correspond to the statistical standard error of the measured atomic fractions in the APT datasets, calculated based on binomial counting statistics from the detected ion counts.

size of APT specimens, diffusible H can readily reach a surface and get desorbed during specimen preparation. Consequently, we infer that the observed H enrichment can originate only from its strong trapping at microstructural defects within the MC carbide. In this regard, C vacancies provide the most likely deep trapping sites for H as they are known to be the most prevalent defects in MC carbides[27].

Vacancy-driven hydrogen–carbide interactions

To validate the H-trapping effect of C vacancies within MC carbides, density functional theory (DFT) calculations were performed, and the results are shown in Extended Data Fig. 7c. In pristine NbC and TiC, H incorporation is energetically unfavourable, with strongly positive binding energies of 2.20 eV and 1.36 eV, respectively, relative to H in octahedral interstitial sites in the adjacent fcc Ni lattice. However, introducing a C vacancy into the carbides markedly stabilizes H, reducing the binding energies to −0.17 eV (for $Nb_{32}C_{31}$) and −1.00 eV (for $Ti_{32}C_{31}$). Motivated by the TEM results shown in Fig. 4c and Extended Data Fig. 5, we further evaluated H in M_6C_5 ($C2/m$ space group), with M_2C ($Fd\bar{3}m$ space group) included for comparison. As shown in Fig. 5a,b, H binding energies in these vacancy-ordered carbides are consistently negative, ranging from −0.19 to −1.00 eV per H, depending on the metal species, vacancy concentration and H occupancy.

These results underscore the propensity for H uptake in vacancy-ordered carbides. Next, we unravel the effects of H on the observed carbide transitions (from MC to M_6C_5, as shown in Fig. 4c) by assessing the Gibbs free energy change (ΔG), or the thermodynamic feasibility, of the following reaction:

$$2.5\,(1-x)H_2 + MC \rightarrow MC_xH_{1-x} + (1-x)CH_4 \qquad (1)$$

Assuming a fixed H_2 partial pressure of 2 MPa, we examined various pressures (from 0.01 to 100 MPa) of CH_4, the reaction by-product. As shown in Fig. 5c, ΔG increases with temperature, and the formations of both Nb_6C_5H and Ti_6C_5H are thermodynamically favourable at 400 °C ($\Delta G < 0$). As further quantified in Fig. 5d, the equilibrium methane pressure (at $\Delta G = 0$) decreases with temperature, reaching ~0.4 GPa at 400 °C for the M_6C_5H system. Such high-pressure methane could aggregate at the carbide–matrix phase boundaries, potentially

https://doi.org/10.1038/s41563-026-02680-w

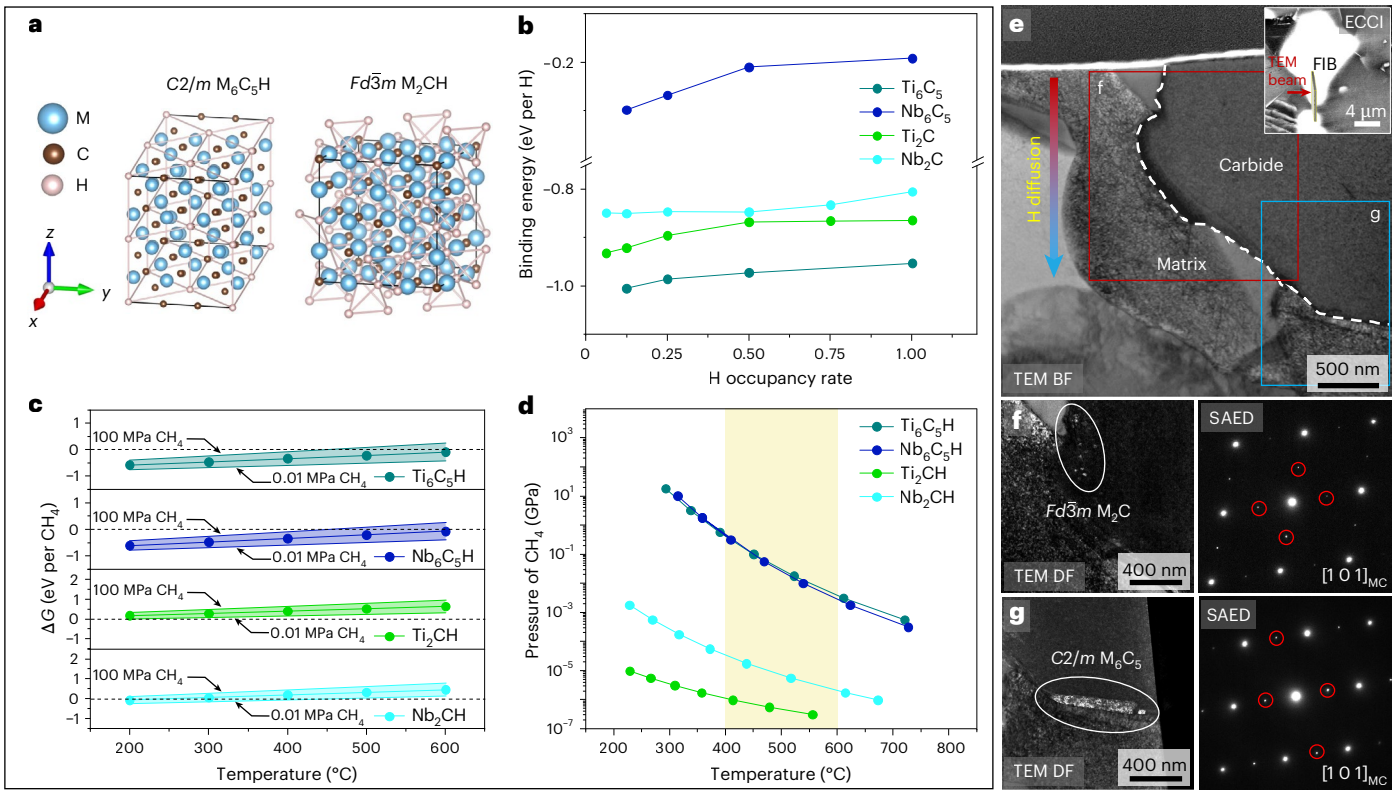

Fig. 5 | Thermodynamics and experimental validation of H-vacancy interactions at elevated temperatures. a, Atomic configurations of H-filled vacancy-ordered carbides, M_6C_5H and M_2CH. **b**, Variation in binding energy per H atom as a function of H occupancy rate in C vacancies in M_6C_5 and M_2C. **c**, Gibbs free energy change (ΔG) for the H-induced formation of CH_4 and H-filled vacancy-ordered carbides, calculated at a fixed H_2 partial pressure of 2 MPa and varying CH_4 pressures (the point-line represents 1 MPa CH_4, and the shaded zone represents 0.01–100 MPa CH_4). **d**, Equilibrium CH_4 pressure at $\Delta G = 0$, calculated with a fixed H_2 partial pressure of 2 MPa. The shaded yellow band indicates the experimental temperature range (400–600 °C). **e**, Bright-field TEM image of carbide (surrounded by the white dotted line) and γ-matrix with an arrow indicating the H diffusion direction; the inset ECCI map illustrates the location where the FIB sample was lifted after H exposure for 0.5 h at 400 °C. **f**,**g**, Dark-field TEM images of newly formed carbides, taken from the red (**f**) and blue (**g**) boxes marked in **e**. The corresponding SAED pattern shows the distinctive diffraction caused by M_2C and M_6C_5, and the red circles mark the superlattice diffraction spots corresponding to the dark-field images. Diffraction patterns acquired from other, different zone axes ($[112]_{MC}$ and $[001]_{MC}$ for M_2C, $[013]_{MC}$ and $[001]_{MC}$ for M_6C_5) are shown in Extended Data Fig. 9.

contributing to the damage nucleation even without external stresses, as observed in Fig. 3c.

The DFT calculations reveal a clear thermodynamic propensity for H to react with MC carbides at 400 °C. Further, our calculations in Extended Data Fig. 8 show that this reaction is thermodynamically less favourable ($\Delta G > 0$ for most modelling scenarios) in the absence of H trapping in C vacancies, demonstrating the crucial role of H-vacancy interactions in the carbide transition. To further validate the occurrence of a H-induced carbide transition, we exposed a freshly polished sample directly to 2 MPa H_2 at 400 °C, allowing a sufficient interaction between H and MC carbides near the sample surface. We maintained a charging time of ~0.5 h, which is the same as during the in situ tensile testing. Subsequently, the cross-section of the carbides was imaged, as shown in Fig. 5e. H-induced carbide C depletion and associated structure transitions are again observed particularly close to the carbide–matrix interface. We further find that the specific type of transformed carbide (Fig. 5f,g and Extended Data Fig. 9) varies with sample depth, which is expected to possess different H concentrations arising from varying diffusion distances. More specifically, diffraction patterns acquired from three different zone axes reveal that M_2C-type carbides form near the sample surface (Fig. 5f and Extended Data Fig. 9a) where H ingress occurs earliest, whereas M_6C_5-type carbides are more prevalent at deeper areas (Fig. 5g and Extended Data Fig. 9b), where H concentration and interaction time with carbides decay. These results further reveal that, in addition to the thermodynamic driving force, the specific resulting structural phase transitions (M_6C_5 or M_2C) resulting from the H–carbide interactions are also influenced by kinetic factors, such as H mobility, localized H abundance (partial pressure) and the associated interaction time.

Discussion of damage mechanisms

Hydrogen-induced interface cracking is commonly attributed to the H-enhanced decohesion mechanism, typically operative at room or cryogenic temperatures[7,9]. This mechanism describes a reduction in interatomic cohesive strength as a function of H coverage of the interface[33,34]. However, reports have shown that the H-trapping effect of various types of interfaces generally decreases as a function of temperature[14,35]. To give an example, our DFT calculations (Extended Data Fig. 7c) suggest only a 6% occupation probability of H atoms at grain-boundary trapping sites in pure Ni under the current testing temperature of 400 °C. We also note that carbide interface cracking can occur with only H charging, that is, without any external mechanical loading (Fig. 3b,c). This finding further weakens the possibility of atomic-H-segregation-induced interface decohesion, which is typically triggered by a critical stress that exceeds the cohesive strength of the interface[36]. We thus attribute the observed carbide–matrix interface cracking to the H-induced carbide transition at elevated temperatures, which leads to the formation of pressurized methane and thus interface weakening. Under external mechanical loading, this process can be further promoted, as stress

concentrations at localized microstructural sites and crack-tip regions can effectively facilitate H diffusion and accumulation[37]. Note that the thermodynamic analysis presented in Fig. 5c indicates that the H-induced carbide transition and methane formation become progressively unfavourable at higher temperatures, a feature that can be supported by our damage analysis of the sample after H exposure at 600 °C (Extended Data Fig. 10). This explains why such a H-induced degradation effect was not observed at higher testing temperatures (for example, 600 °C for the studied alloy; Extended Data Fig. 2d).

We note that the proposed H-induced damage mechanism in the studied Ni-based alloy differs from the high-temperature H attack previously documented and discussed for the case of carbon steels. For the latter mechanism, H primarily interacts with solute C atoms in the steel matrix, leading to localized C depletion that may induce the dissolution of carbides (commonly Fe_3C)[15–17]. Here we highlight a vacancy-driven direct chemical reaction between H and carbides that occurs near the carbide–matrix interface, thereby stimulating damage nucleation at this interface rather than within the matrix or at grain boundaries, as often reported in the high-temperature H-attack of carbon steels[15,17]. To further demonstrate the generality and damaging effects of the proposed mechanism, we examined another Ni-based superalloy (directionally solidified CM247LC) containing (Ta,Hf)C carbides. The H-induced carbide transition and the associated debonding of the carbide–matrix interface are again observed at elevated temperatures (Supplementary Fig. 3). Compared with the presented IN718, which contains only ~0.2 vol% MC carbides, CM247LC exhibits a much higher carbide fraction of ~1.7 vol% (Supplementary Fig. 3), leading to a more pronounced reduction of ductility in the presence of H (~63.8%; Supplementary Fig. 3). Such a correlation between the extent of H embrittlement and the carbide fraction further validates the proposed damage mechanism, distinguishing it from the conventionally discussed high-temperature H-attack effect, which scales mainly with the matrix C content[18].

To conclude, we unravel the damage mechanisms of Ni-based carbide-containing alloys in a H atmosphere at elevated temperatures, where H ingress into the vacancies of metal carbides promotes their structure transition, accompanied by pressurized methane release, ultimately leading to damage initiation (Supplementary Fig. 4). This degradation pathway contrasts with the H-induced damage mechanisms reported for lower ambient temperatures, where failure is typically governed by intergranular or cleavage-like fracture due to the physical interactions between H and intrinsic defects like grain boundaries and dislocations[7,9]. While these defects act as effective H traps at low temperatures[10–12], their trapping capacity diminishes rapidly with increasing temperature (Extended Data Fig. 7c). By contrast, vacancy-ordered carbides retain their strong H-trapping ability even at 400 °C (Extended Data Fig. 7c), underscoring an interaction and degradation mechanism that becomes dominant when the energetically shallow trapping sites lose effectiveness. These findings provide mechanistic insights into the service performance of Ni-based superalloys—the most important class of structural backbone materials used in the hot sections of H_2-fuelled energy-conversion systems and infrastructure—as well as other carbide-containing alloys, including steels and metal–ceramic composites. These insights can also lay a scientific foundation for the future development of predictive models and damage-tolerant high-temperature materials, which are essential to guide and equip the coming H_2-fuelled sustainable gas-turbine energy, combustion and air-traffic systems.

Online content

Any methods, additional references, Nature Portfolio reporting summaries, source data, extended data, supplementary information, acknowledgements, peer review information; details of author contributions and competing interests; and statements of data and code availability are available at https://doi.org/10.1038/s41563-026-02680-w.

References

1. Pashchenko, D. Hydrogen-rich gas as a fuel for the gas turbines: a pathway to lower CO_2 emission. *Renew. Sustain. Energy Rev.* **173**, 113117 (2023).
2. Adler, E. J. & Martins, J. R. R. A. Hydrogen-powered aircraft: fundamental concepts, key technologies, and environmental impacts. *Prog. Aerosp. Sci.* **141**, 100922 (2023).
3. International Energy Agency. *Global Energy Review 2025* https://www.iea.org/reports/global-energy-review-2025 (International Energy Agency, 2025).
4. Lufthansa Technik. Hydrogen Aviation Lab https://www.lufthansa-technik.com/en/hydro-lab (accessed 1 April 2026).
5. Kovaleva, M. et al. The evaluation of ammonia/hydrogen combustion on the H permeation and embrittlement of nickel-base superalloys. In *Proc. ASME Turbo Expo 2022: Turbomachinery Technical Conference and Exposition* https://doi.org/10.1115/GT2022-82239 (ASME, 2022).
6. Prameela, S. E. et al. Materials for extreme environments. *Nat. Rev. Mater.* **8**, 81–88 (2023).
7. Lynch, S. Hydrogen embrittlement phenomena and mechanisms. *Corros. Rev.* **30**, 105–123 (2012).
8. Raabe, D., Tasan, C. C. & Olivetti, E. A. Strategies for improving the sustainability of structural metals. *Nature* **575**, 64–74 (2019).
9. Sun, B. et al. Current challenges in the utilization of hydrogen energy-a focused review on the issue of hydrogen-induced damage and embrittlement. *Adv. Appl. Energy* **14**, 100168 (2024).
10. Zhou, X., Marchand, D., McDowell, D. L., Zhu, T. & Song, J. Chemomechanical origin of hydrogen trapping at grain boundaries in fcc metals. *Phys. Rev. Lett.* **116**, 075502 (2016).
11. Tang, Y. & El-Awady, J. A. Atomistic simulations of the interactions of hydrogen with dislocations in fcc metals. *Phys. Rev. B* **86**, 174102 (2012).
12. You, Y.-W. et al. Dissolving, trapping and detrapping mechanisms of hydrogen in bcc and fcc transition metals. *AIP Adv.* **3**, 012118 (2013).
13. Gavriljuk, V. G., Shyvaniuk, V. M. & Teus, S. M. Hydrogen-dislocation interaction in relation to hydrogen embrittlement and enhanced plasticity of metals. *Int. J. Hydrogen Energy* **50**, 352–360 (2024).
14. Leitner, S., Ecker, W., Fischer, F. D. & Svoboda, J. Thermodynamic trapping and diffusion model for multiple species in systems with multiple sorts of traps. *Acta Mater.* **233**, 117940 (2022).
15. Weiner, L. C. Kinetics and mechanism of hydrogen attack of steel. *Corrosion* **17**, 109–115 (1961).
16. Nelson, H. G. Hydrogen embrittlement. *Treat. Mater. Sci. Technol.* **8**, 327–357 (1983).
17. Shewmon, P. G. Hydrogen attack of pressure-vessel steels. *Mater. Sci. Technol.* **1**, 2–11 (1985).
18. Poorhadari, K. A comprehensive examination of high-temperature hydrogen attack—a review of over a century of investigations. *J. Mater. Eng. Perform.* **30**, 7875–7908 (2021).
19. Zhou, X., Tehranchi, A. & Curtin, W. A. Mechanism and prediction of hydrogen embrittlement in fcc stainless steels and high entropy alloys. *Phys. Rev. Lett.* **127**, 175501 (2021).
20. Lee, J. A. *Hydrogen Embrittlement*Report No. NASA/TM-2016-218602 (NASA, 2016).
21. Reed, R. C. *The Superalloys: Fundamentals and Applications* (Cambridge Univ. Press, 2008).
22. Hong, S. J., Chen, W. P. & Wang, T. W. A diffraction study of the γ″ phase in INCONEL 718 superalloy. *Metall. Mater. Trans. A* **32**, 1887–1901 (2001).
23. Anderson, M., Thielin, A.-L., Bridier, F., Bocher, P. & Savoie, J. δ Phase precipitation in Inconel 718 and associated mechanical properties. *Mater. Sci. Eng. A* **679**, 48–55 (2017).

24. Ruan, J. J., Ueshima, N. & Oikawa, K. Phase transformations and grain growth behaviors in superalloy 718. *J. Alloys Compd.* **737**, 83–91 (2018).
25. Thuvander, M. et al. Quantitative atom probe analysis of carbides. *Ultramicroscopy* **111**, 604–608 (2011).
26. Peng, Z., Choi, P.-P., Gault, B. & Raabe, D. Evaluation of analysis conditions for laser-pulsed atom probe tomography: example of cemented tungsten carbide. *Microsc. Microanal.* **23**, 431–442 (2017).
27. Gusev, A. I., Rempel, A. A. & Magerl, A. J. *Disorder and Order in Strongly Nonstoichiometric Compounds: Transition Metal Carbides, Nitrides and Oxides* (Springer, 2013).
28. Max, B. et al. Atomic species associated with the Portevin–Le Chatelier effect in superalloy 718 studied by mechanical spectroscopy. *Metall. Mater. Trans. A* **49**, 2057–2068 (2018).
29. Tarzimoghadam, Z. et al. Multi-scale and spatially resolved hydrogen mapping in a Ni–Nb model alloy reveals the role of the δ phase in hydrogen embrittlement of alloy 718. *Acta Mater.* **109**, 69–81 (2016).
30. Epicier, T., Acevedo, D. & Perez, M. Crystallographic structure of vanadium carbide precipitates in a model Fe–C–V steel. *Philos. Mag.* **88**, 31–45 (2008).
31. Chang, Y. et al. Ti and its alloys as examples of cryogenic focused ion beam milling of environmentally-sensitive materials. *Nat. Commun.* **10**, 942 (2019).
32. Gault, B. et al. Towards establishing best practice in the analysis of hydrogen and deuterium by atom probe tomography. *Microsc. Microanal.* **30**, 1205–1220 (2024).
33. Pfeil, L. B. The effect of occluded hydrogen on the tensile strength of iron. *Proc. R. Soc. Lond. A* **112**, 182–195 (1926).
34. Troiano, A. R. The role of hydrogen and other interstitials in the mechanical behavior of metals. *Trans. Am. Soc. Met.* **52**, 54–81 (1960).
35. Mai, H. L., Cui, X.-Y., Scheiber, D., Romaner, L. & Ringer, S. P. An understanding of hydrogen embrittlement in nickel grain boundaries from first principles. *Mater. Des.* **212**, 110283 (2021).
36. Liang, Y. & Sofronis, P. Toward a phenomenological description of hydrogen-induced decohesion at particle/matrix interfaces. *J. Mech. Phys. Solids* **51**, 1509–1531 (2003).
37. Oriani, R. A. The diffusion and trapping of hydrogen in steel. *Acta Metall.* **18**, 147–157 (1970).
38. Guéret, C., Daroux, M. & Billaud, F. Methane pyrolysis: thermodynamics. *Chem. Eng. Sci.* **52**, 815–827 (1997).
39. Vijayvargia, K. et al. On the chemomechanics of bubble growth in hydrogen attack of plain carbon steels. *Corros. Sci.* **253**, 112999 (2025).

Methods

Materials

The as-cast ingot of the IN718 alloy was initially fabricated by a combination of vacuum induction melting, electro slag remelting and vacuum arc remelting. The ingot was then radially forged into a disc with a diameter of 285 mm. Cylindrical blanks (17 mm in diameter and 130 mm in length) were sectioned from the disc in the radial direction via electrical discharge machining for heat treatment. These blanks underwent solution treatment at 960 °C for 1 h and cooled in air. They were subsequently aged at 720 °C for 8 h, followed by furnace cooling at 50 °C h^{-1} to 620 °C, then aged at 620 °C for a further 8 h and finally cooled in air.

Hydrogen charging and mechanical testing

Hydrogen charging and mechanical tests were conducted on a self-developed servo motor testing machine equipped with a high-temperature and high-pressure H gas chamber. Two distinct sample geometries were employed for tensile testing: cylindrical samples (10.2 mm gauge length and 6.0 mm diameter) and plate samples (10.2 mm gauge length, 8.0 mm width and 3.0 mm thickness). All sample surfaces were mechanically ground with silicon carbide paper to a surface roughness of roughness average (Ra) 0.4 µm, and the plate samples received final polishing to a mirror finish. The applied mechanical load was measured by an internal load cell within the chamber, and real-time strain was monitored using a linear variable displacement transducer. High-purity H_2 and Ar gases (both 99.99%) were used during tensile testing. Prior to each experiment, the chamber was purged multiple times with Ar to reduce the residual oxygen content below 1.0 vol%. A hydrogen pressure of 2 MPa was applied for in situ tensile tests conducted at 25 °C, 200 °C, 400 °C and 600 °C (Fig. 2d and Extended Data Figs. 2 and 3), as well as for H charging experiments (Figs. 3 and 5 and Extended Data Fig. 10a–c). The duration of the tensile tests was 0.5–0.7 h (depending on the total elongation of the samples) at an initial strain rate of ~2.9×10^{-5} s^{-1}, and approximately ~2.0 h at a slower initial strain rate of ~1.3×10^{-5} s^{-1}. The H charging experiments lasted approximately 0.5 h, consistent with the in situ tensile tests conducted at 400 °C and initial strain rate of ~2.9×10^{-5} s^{-1}.

Microstructure observations

The characterization of the microstructure and damage was performed using a field-emission SEM instrument (Zeiss Gemini 460) equipped with an EBSD detector (Symmetry S2, Oxford Instruments) and an EDX spectrometer. EBSD data were analysed using the TSL-OIM software package. Samples for EBSD and ECCI were prepared by mechanical grinding and polishing to achieve a mirror finish. Site-specific TEM lamellae, focusing on carbide–matrix interfaces and adjacent regions, were obtained using FIB lift-out techniques (Zeiss Gemini Crossbeam 350). TEM characterization was conducted using an FEI Talos F200X (accelerating voltage, E_p = 200 kV), using different probing currents for different probing purposes: 10 pA for SAED, 0.3–0.6 nA for bright-field and dark-field imaging, 1.6 nA for high-resolution TEM imaging, 2.5 nA for EDX mapping and 1.7 nA for high-angle annular dark-field scanning TEM (HAADF-STEM) imaging. Additional low-dose imaging was performed on an aberration-corrected Thermo Fisher Themis Z TEM instrument, using a probe current of 7 pA for SAED and bright-field images and 3 pA for HAADF-STEM imaging.

APT experiments and analysis

The APT specimens were site-specifically prepared at the partially cracked carbide–matrix interfaces using a dual-beam FIB SEM device. A standard lift-out protocol was implemented for specimen preparation[40]. A subsequent fabrication process for a needle-shaped specimen was carried out in a cryogenically cooled FIB (−190 °C, Thermo Fisher Helios 5 CX Gallium FIB SEM instrument, Aquilos cryo-stage), aiming to minimize H ingress and undesired hydride formation. The measurements were conducted using a local electrode atom probe (LEAP 5000 XR, Cameca Instruments) at −223 °C. Data acquisition was carried out in high-voltage laser pulsing mode with a laser energy of 45 pJ. The pulsing repetition rate was set to 125 kHz, and the detection rate was controlled at 0.5% (five ions in every 1,000 pulses). The collected APT data were reconstructed using the AP Suite v.6.1 software.

Precisely measuring carbon concentrations in carbides by APT has been reported to be particularly challenging[25,26,41] because of possible overlaps between mass peaks[25], for example, C_2^{2+} and C_1^+ or C_4^{2+} and C_2^+, as well as losses due to ion pile-up at the detector[42], partly arising from molecular ion dissociations[43]. Here the isotopic ratios have been measured to ensure that the measurement was as accurate as possible. In contrast to the natural abundance of C ($^{12}C \approx 98.9\%$ and $^{13}C \approx 1.1\%$)[44], the isotopic ratios of C were measured to be 65 ($^{12}C \approx 10.07\%$ and $^{13}C \approx 0.156\%$), suggesting that the C concentration might be underestimated due to the aforementioned spectral overlaps and multi-hit loss effects. We further assessed the field conditions across different carbide measurements. The overlaps among the probed carbides, as indicated by the multiple charge state ratio, $\mathrm{Log}_{10}^{Cr^+/(Cr^{2+}+Cr^+)}$, reveals a consistent and narrow field range of 21.38 V nm^{-1} to 22.77 V nm^{-1} (ref. 45). This consistency fills us with confidence that, even if some of the C from the molecular clusters is underestimated, the qualitative assessment of the C content between the carbide measurements before and after in situ tensile testing under 2 MPa H_2 at 400 °C remains reliably comparable. The detailed analyses are provided in Supplementary Fig. 1a.

The origin of the detected H, either from residual chamber gas or solute H within the sample, can be qualitatively accessed by the local electrode field strength, which can be estimated using the charge state ratio in accordance with post-ionization theory[45]. It has been reported that a higher local electrical field is likely to result in a lower amount of H from residual gas[46,47]. Focusing on Supplementary Fig. 1b, the notably higher ratios of Cr^{2+}/Cr^+ and H^+/H_2^+ observed in the carbide, despite the localized fluctuations, indicate a relatively high electric field in this phase, and vice versa in the fcc matrix. This variation in field strength strongly suggests that the H atoms detected in carbides primarily originate from solute H actually within the sample, without much contribution from the residual gas from the atom probe chamber.

Computational details

This study employed DFT calculations via the Vienna Ab initio Simulation Package[48,49], using the Perdew–Burke–Ernzerhof exchange–correlation functional within the generalized gradient approximation framework[50]. Core–electron interactions were treated using the projector augmented-wave method[51]. A plane-wave cut-off energy of 500 eV was applied, with Brillouin zone sampling performed using the Γ-centred Monkhorst–Pack scheme. The investigated systems include carbide phases MC_x (M = Nb, Ti) with the following configurations: for the MC ($Fm\bar{3}m$ space group) phase, a 2 × 2 × 2 supercell (64 atoms) and a 4 × 4 × 4 k-point grid were used; for the M_2C phase ($Fd\bar{3}m$ space group), a 2 × 1 × 1 supercell (96 atoms) with a 2 × 4 × 4 k-point grid was employed; and for the M_6C_5 phase ($C2/m$ space group) a 2 × 1 × 2 supercell (88 atoms) with a 3 × 4 × 3 k-point grid was used. For thermodynamic evaluations, all C vacancies (octahedral interstitial sites) in the MC_xH_{1-x} systems were assumed to be fully occupied by H atoms. Convergence criteria were uniformly set as follows: electronic self-consistency threshold of 10^{-8} eV per atom, ionic relaxation force threshold of 0.01 eV $Å^{-1}$ and phonon calculation force threshold of 10^{-6} eV $Å^{-1}$.

For a H-containing metal carbide, $M_xC_yH_z$, the H binding energy was calculated as follows:

$$E_b = \left(E_{M_xC_yH_z} - E_{M_xC_y}\right)/z - \left(E_{NiH} - E_{Ni}\right) \quad (2)$$

where $E_{M_xC_yH_z}$ and $E_{M_xC_y}$ represent the energy of the carbide with and without H insertion, respectively, and z is the number of H atoms. E_{NiH}

and E_{Ni} denote the total energies of a Ni supercell with and without a single H atom occupying an octahedral interstitial site, respectively. All H-related calculations include zero-point energy corrections.

The Gibbs free energy was calculated to assess the thermodynamic feasibility of reactions at finite temperatures using the following expression:

$$G = E_0 + F_{vib} + F_{ele} + F_{trans} + F_{rot} + PV \quad (3)$$

where E_0 is the total energy at 0 K, F_{vib} accounts for lattice vibrational contributions via the quasi-harmonic approximation[52] and F_{ele} incorporates electronic thermal excitations with the Fermi–Dirac distribution[53]. The terms F_{trans} and F_{rot} denote the translational and rotational free energies, respectively, and are applied only to gaseous species (H_2 and CH_4). The PV term is evaluated using the ideal gas equation of state (P, pressure; V, volume), which should be sufficiently accurate at our experimental pressure of 2 MPa (refs. 54,55). For solid carbides, the PV contribution is negligible due to their high modulus ($\Delta PV < 10^{-4}$ eV per atom for $\Delta P < 1$ GPa) and is thus not explicitly included. Free energy calculations were performed using density functional perturbation theory in combination with the Phonopy package[54,56] and the Shermo software[57]. Visualization was performed using the VESTA software package[58].

Data availability

Source data are provided with this paper. Any additional data are available from the corresponding authors.

References

40. Thompson, K. et al. In situ site-specific specimen preparation for atom probe tomography. *Ultramicroscopy* **107**, 131–139 (2007).
41. Sha, W., Chang, L., Smith, G. D. W., Cheng, L. & Mittemeijer, E. J. Some aspects of atom-probe analysis of Fe–C and Fe–N systems. *Surf. Sci.* **266**, 416–423 (1992).
42. Peng, Z. et al. On the detection of multiple events in atom probe tomography. *Ultramicroscopy* **189**, 54–60 (2018).
43. Peng, Z. et al. Unraveling the metastability of C_n^{2+} (n=2–4) clusters. *J. Phys. Chem. Lett.* **10**, 581–588 (2019).
44. Meija, J. et al. Isotopic compositions of the elements 2013 (IUPAC technical report). *Pure Appl. Chem.* **88**, 293–306 (2016).
45. Kingham, D. R. The post-ionization of field evaporated ions: a theoretical explanation of multiple charge states. *Surf. Sci.* **116**, 273–301 (1982).
46. Kellogg, G. L. Pulsed laser stimulated field desorption of hydrogen from molybdenum. *J. Chem. Phys.* **74**, 1479–1487 (1981).
47. Chang, Y. et al. Characterizing solute hydrogen and hydrides in pure and alloyed titanium at the atomic scale. *Acta Mater.* **150**, 273–280 (2018).
48. Kresse, G. & Hafner, J. *Ab initio* molecular dynamics for open-shell transition metals. *Phys. Rev. B* **48**, 13115–13118 (1993).
49. Kresse, G. & Hafner, J. *Ab initio* molecular dynamics for liquid metals. *Phys. Rev. B* **47**, 558(R)–561(R) (1993).
50. Perdew, J. P., Burke, K. & Ernzerhof, M. Generalized gradient approximation made simple. *Phys. Rev. Lett.* **77**, 3865–3868 (1996).
51. Blöchl, P. E. Projector augmented-wave method. *Phys. Rev. B* **50**, 17953–17979 (1994).
52. Togo, A. & Tanaka, I. First principles phonon calculations in materials science. *Scr. Mater.* **108**, 1–5 (2015).
53. Mermin, N. D. Thermal properties of the inhomogeneous electron gas. *Phys. Rev.* **137**, A1441–A1443 (1965).
54. Odette, G. R. & Vagarali, S. S. An equation-of-state for methane for modeling hydrogen attack in ferritic steels. *Metall. Trans. A* **13**, 299–303 (1982).
55. Hagelstein, P. L. Equation of state and fugacity models for H_2 and for D_2. *J. Condensed Matter. Nucl. Sci.* **16**, 23–45 (2015).
56. Baroni, S., de Gironcoli, S., Dal Corso, A. & Giannozzi, P. Phonons and related crystal properties from density-functional perturbation theory. *Rev. Mod. Phys.* **73**, 515–562 (2001).
57. Lu, T. & Chen, Q. Shermo: a general code for calculating molecular thermochemistry properties. *Comput. Theor. Chem.* **1200**, 113249 (2021).
58. Momma, K. & Izumi, F. VESTA 3 for three-dimensional visualization of crystal, volumetric and morphology data. *J. Appl. Crystallogr.* **44**, 1272–1276 (2011).

Acknowledgements

We thank L. Liu for the technical support with H charging and mechanical testing and acknowledge D. Xie, D. Ponge and W. Ming for fruitful discussions. We thank W. Li and S. Dai for the assistance with the TEM experiments. Parts of the SEM and EBSD experiments were performed at the Liaoning Academy of Materials. We thank the Hefei Advanced Computing Center for providing computing resources.

Author contributions

B.S. and X.-C.Z. conceived the project. S.K. and B.S. designed the research. S.K. prepared the material, characterized the microstructure and conducted H-charging and tensile tests. S.K., B.S. and Y.Z. analysed the SEM and TEM results. X.D. performed the APT experiments. X.D., A.S. and B.G. discussed and interpreted the APT results. Z.Z. and J.H. performed the DFT calculations. B.S., X.-C.Z., D.R. and S.-T.T. supervised the study. S.K., B.S., Z.Z. and J.H. wrote the manuscript. B.S., X.D., S.W., B.G., D.R. and S.-T.T revised the manuscript. All authors discussed the results and commented on the manuscript.

Funding

This work was supported by the National Natural Science Foundation of China (no. U25A20188, no. 52130511, no. 52275147 and no. U2572212), National Key Research and Development Project (no. 2023YFB3712103), Key Research and Development Program of Shandong Province (no. 2024CXPT064) and Shanghai Gaofeng Project for University Academic Program Development. B.S. and X.-C.Z. disclose support for the research of this work from New Cornerstone Science Foundation through the Xplorer Prize. Open access funding provided by Max Planck Society.

Competing interests

The authors declare no competing interests.

Additional information

Extended data is available for this paper at https://doi.org/10.1038/s41563-026-02680-w.

Supplementary information The online version contains supplementary material available at https://doi.org/10.1038/s41563-026-02680-w.

Correspondence and requests for materials should be addressed to Binhan Sun, Xian-Cheng Zhang or Dierk Raabe.

Peer review information *Nature Materials* thanks the anonymous reviewers for their contribution to the peer review of this work.

https://doi.org/10.1038/s41563-026-02680-w

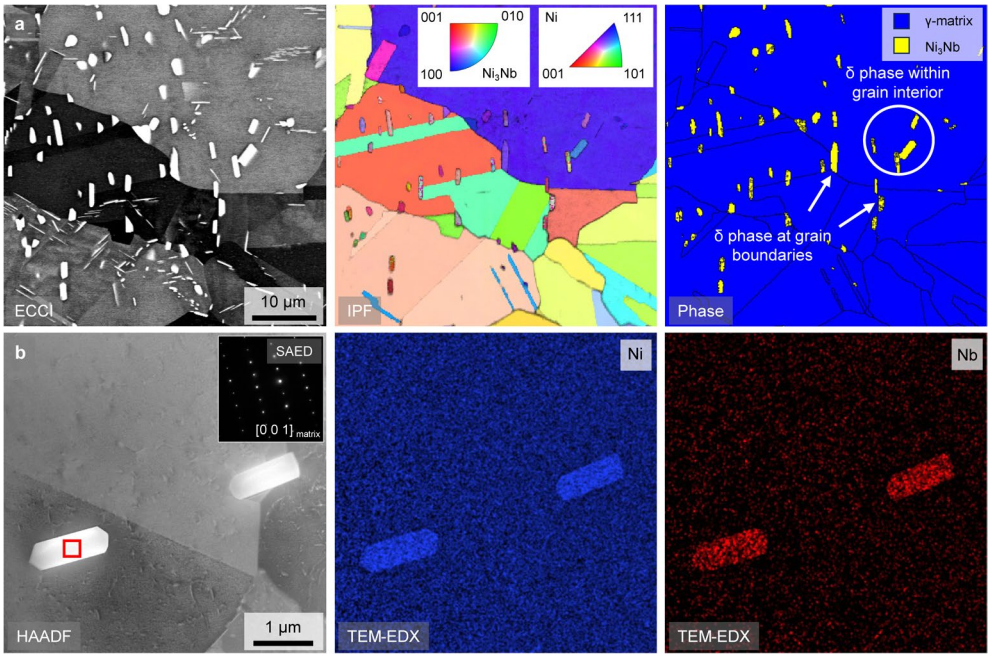

Extended Data Fig. 1 | Distribution, morphology and structure of the δ phase within the studied material IN718. a, Electron channeling contrast imaging (ECCI), electron backscatter diffraction (EBSD) inverse pole figure (IPF) and phase map, showing the distribution of the δ phase. **b**, High-angle annular dark-field scanning transmission electron microscopy (HAADF-STEM) image, showing the morphology of the δ phase. The selected area electron diffraction (SAED) pattern taken from the marked rectangular frame is placed as the inset to reveal the crystal structure (DO_a) of the δ phase. The corresponding energy-dispersive X-ray spectroscopy (EDX) maps of Ni and Nb are placed on the right-hand side.

https://doi.org/10.1038/s41563-026-02680-w

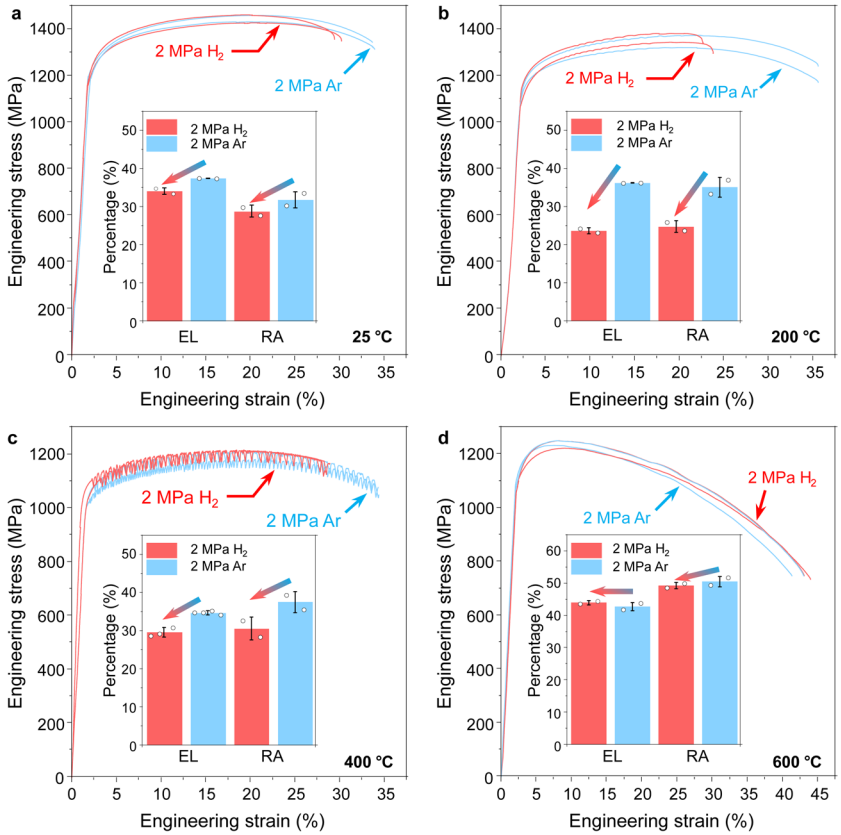

Extended Data Fig. 2 | Tensile stress-strain curves of the material loaded under 2 MPa H_2 and Ar at the strain rate of ~ 2.9×10^{-5} s^{-1}. **a**, 25 °C. **b**, 200 °C. **c**, 400 °C. **d**, 600 °C. Two representative testing curves are shown for each condition. The curves obtained in Ar atmosphere serve as references to reveal the occurrence of H-induced damage and its degradation effect on material's property. The total elongation (EL) and reduction in cross-sectional area (RA) values of samples loaded under 2 MPa H_2 and Ar are inset in each figure. Data are presented as mean values ± SD. Individual white dots represent independent tensile tests (n = 2 for 2 MPa H_2 and Ar at 25 °C, 200 °C and 600 °C; n = 3 for 2 MPa H_2 at 400 °C; n = 4 for 2 MPa Ar at 400 °C). Compared to 25 °C, a more severe reduction in EL and RA was observed at 200 °C, attributed to the higher H trapping rate (as illustrated in Fig. 1d of the manuscript). At higher temperatures (*for example*, 400 °C), the dominant mechanism shifts to H-related chemical reaction with carbides. No notable degradation in tensile properties is observed at 600 °C, as the methane formation becomes thermodynamically less favorable (as supported by DFT calculations in Fig. 5d of the manuscript).

https://doi.org/10.1038/s41563-026-02680-w

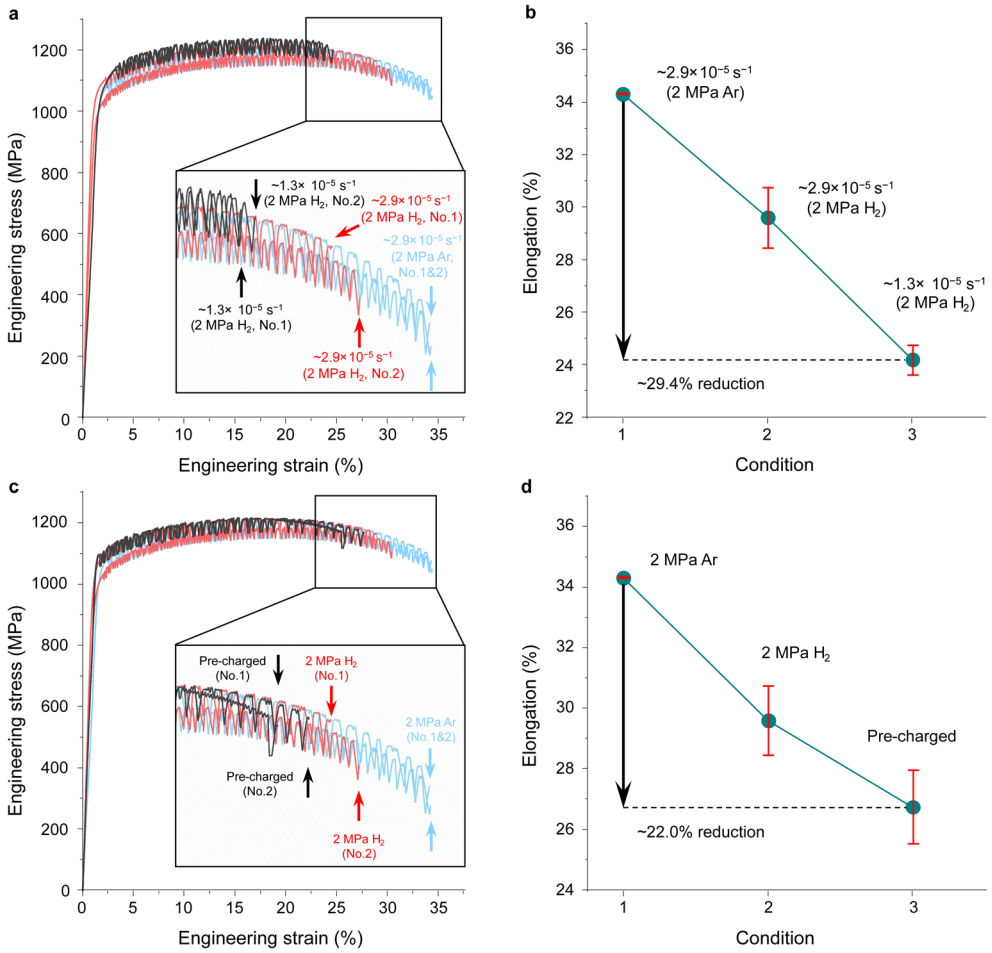

Extended Data Fig. 3 | Tensile properties of specimens tested under 2 MPa Ar and H_2 at 400 °C under different H_2 charging and strain-rate conditions. **a**, Tensile stress–strain curves of specimens tested under 2 MPa Ar and H_2 at different strain rates (two repeated testing results are shown). **b**, Average total elongation values with error bars. Data are presented as mean values ± SD. Individual dots represent independent tensile tests (n = 2 for each condition), corresponding to the repeated testing results shown in **a**. No notable influence of tested strain rates on ductility is observed under Ar environment. At room temperature, the H-induced reduction of total elongation is only ~9.2% at the lower strain rate of ~1.3×10^{-5} s^{-1}. **c**, Tensile stress–strain curves of specimens tested directly under 2 MPa Ar, 2 MPa H_2, and after H pre-charging at 400 °C followed by in situ testing under H_2 exposure (two repeated testing results are shown). **d**, Average total elongation values with error bars. Data are presented as mean values ± SD. Individual dots represent independent tensile tests (n = 2 for each condition), corresponding to the repeated testing results shown in **c**. Specimens for the pre-charged condition were charged in H_2 for 64 h at 400 °C, followed by in situ testing under 2 MPa H_2.

https://doi.org/10.1038/s41563-026-02680-w

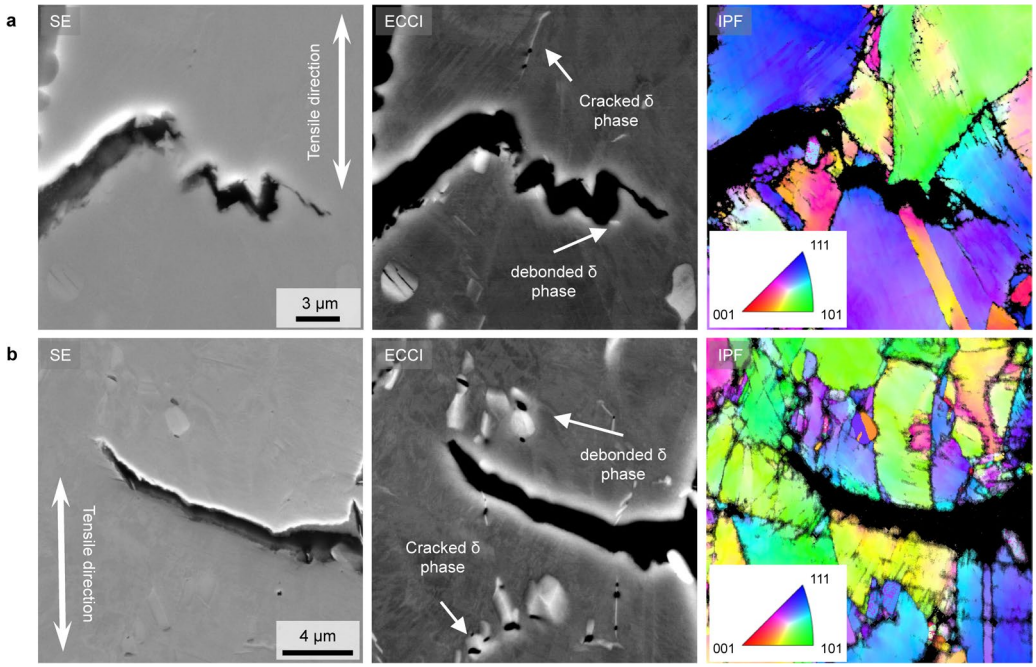

Extended Data Fig. 4 | H-induced damage behavior at 25 °C and 200 °C. **a**, 25 °C. **b**, 200 °C. The secondary electron (SE) images show the representative crack morphology and damage behavior observed after in situ tensile testing under H_2 exposure. Corresponding ECCI and EBSD-IPF maps reveal that damage is formed within the δ phase or at the δ/γ interfaces, which promotes the formation and propagation of intergranular and transgranular cracks (corresponding to the damage mechanisms in the lower temperature regime as indicated in Fig. 1d). Compared with 25 °C, an exacerbated H-induced damage associated with δ phase is observed at 200 °C, due to higher H trapping rate (as described in Fig. 1d).

https://doi.org/10.1038/s41563-026-02680-w

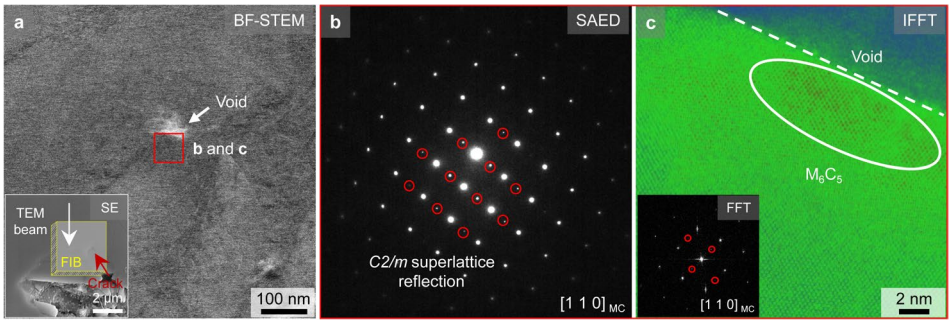

Extended Data Fig. 5 | Additional transmission electron microscopy (TEM) analysis of regions close to carbide-matrix interface that are damaged upon mechanical loading and H_2 exposure at 400 °C. a, The overview bright-field scanning TEM (BF-STEM) image of a cracked carbide-matrix interface, with a SE inset showing the corresponding FIB-lifted area. **b**, Selected area electron diffraction (SAED) pattern taken from the rectangular frame in **a**, showing again superlattice spots that correspond well to the vacancy-ordered M_6C_5-type carbide (*C2/m* space group). **c**, Inverse Fast Fourier Transformation (IFFT) image based on the superlattice reflection spots marked in the inset Fast Fourier Transformation (FFT) image taken from the rectangular frame in **a**, revealing the formation of M_6C_5-type carbide close to the carbide-matrix interfacial void. Probe currents (*Ip*) of ~7 pA for BF-STEM and SAED imaging and of 3 pA for HAADF-STEM imaging were used to prevent any possible electron beam damage to the beam-sensitive newly formed carbide.

https://doi.org/10.1038/s41563-026-02680-w

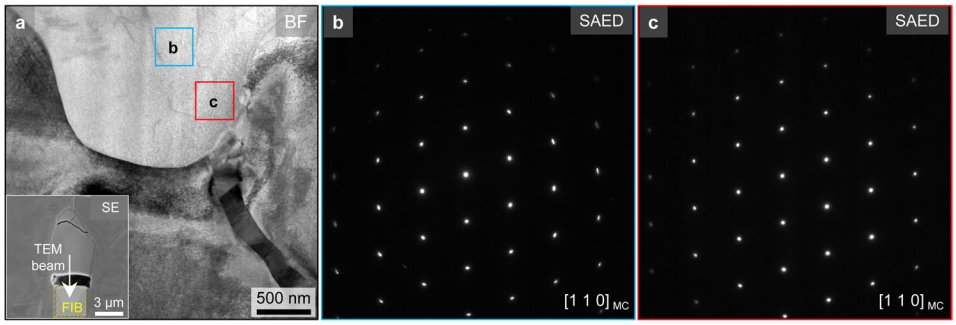

Extended Data Fig. 6 | TEM analysis of regions close to carbide-matrix interface after mechanical loading under Ar atmosphere at 400 °C. a, The overview TEM bright field (BF) image, with a SE inset showing the corresponding FIB-lifted area. **b**,**c**, SAED patterns acquired from regions indicated by the blue and red rectangular frames marked in **a**, respectively. The MC carbide maintains its initial FCC (B1) structure with no superlattice structure observed.

https://doi.org/10.1038/s41563-026-02680-w

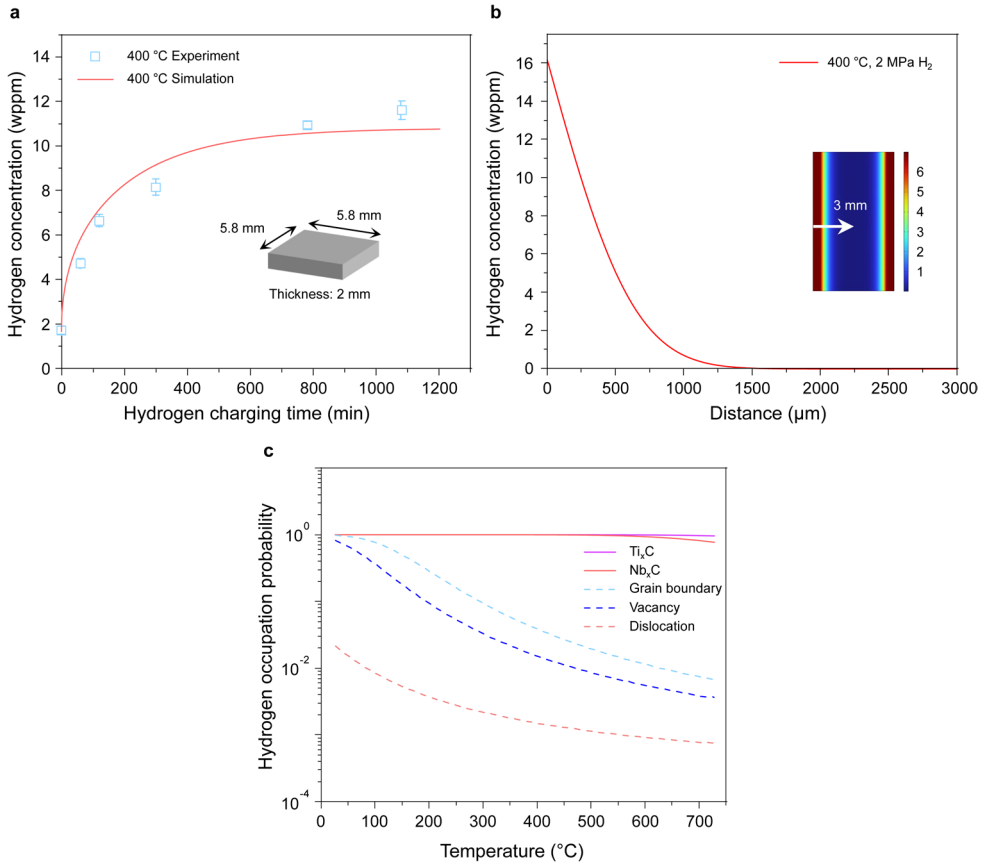

Extended Data Fig. 7 | H concentration and temperature dependence of H occupation probabilities at various defects. a, Experimentally measured H concentration at 400 °C for varying charging times (0, 60, 120, 300, 780 and 1080 min) and the corresponding diffusion analysis, with H-charging sample geometry inset. For each charging time, two independent samples were measured. Data are presented as mean values ± SD. Post-charging samples were immediately quenched in liquid nitrogen following atmosphere venting. The H concentration was measured by hot extraction using a LECO ONH836 analyzer (calibrated using steel pin standards containing 6.9 wppm diffusible H). **b**, Simulated H distribution after 0.5 h charging under 2 MPa H_2 at 400 °C. The calculation methods are detailed in Supplementary Note 1. The inset shows the H concentration contour map, with the sample radius labelled as 3 mm. The penetration depth reaches approximately 1500 μm. **c**, The occupation probability P_i of H at defect site i is calculated using the relation $P_i = 1/[1+exp(-E_b^i/k_BT)/c_0]$, where $c_O = 4.8$ wppm, E_b^i denotes the maximum H binding energies at each defect type, k_B is the Boltzmann constant and T is the temperature. Values of E_b^i for grain boundaries, vacancies, and dislocations are adopted from Refs. 10–12.

https://doi.org/10.1038/s41563-026-02680-w

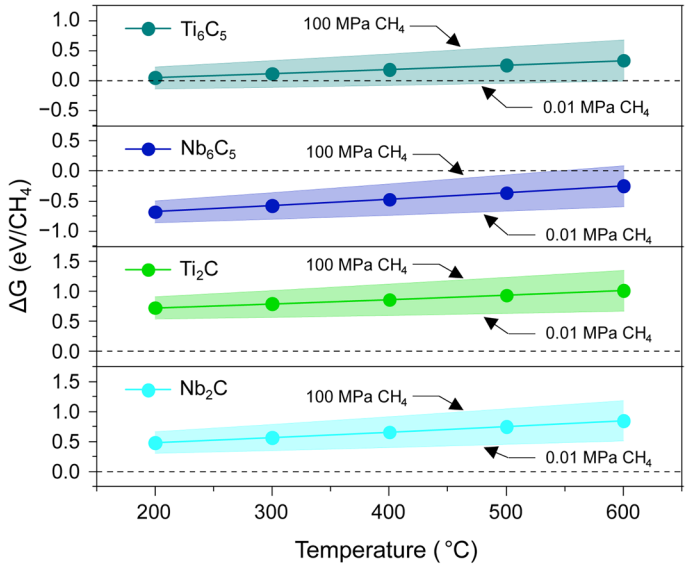

Extended Data Fig. 8 | Thermodynamics of H-carbide interaction without H uptake in C vacancies within carbides. Gibbs free energy change (ΔG) for the H-induced formation of CH_4 and vacancy-ordered carbides without H occupation, calculated at a fixed H_2 partial pressure of 2 MPa and varying CH_4 pressures (the point-line represents 1 MPa CH_4, shaded zone represents 0.01–100 MPa CH_4). The ΔG was evaluated considering the reaction: $2(1-x)H_2 + MC \rightarrow MC_x + (1-x)CH_4$. This reaction is thermodynamically less favorable (ΔG > 0 for most modelling scenarios) in the absence of H uptake in C vacancies, compared to the DFT calculations shown in Fig. 5c of the manuscript.

https://doi.org/10.1038/s41563-026-02680-w

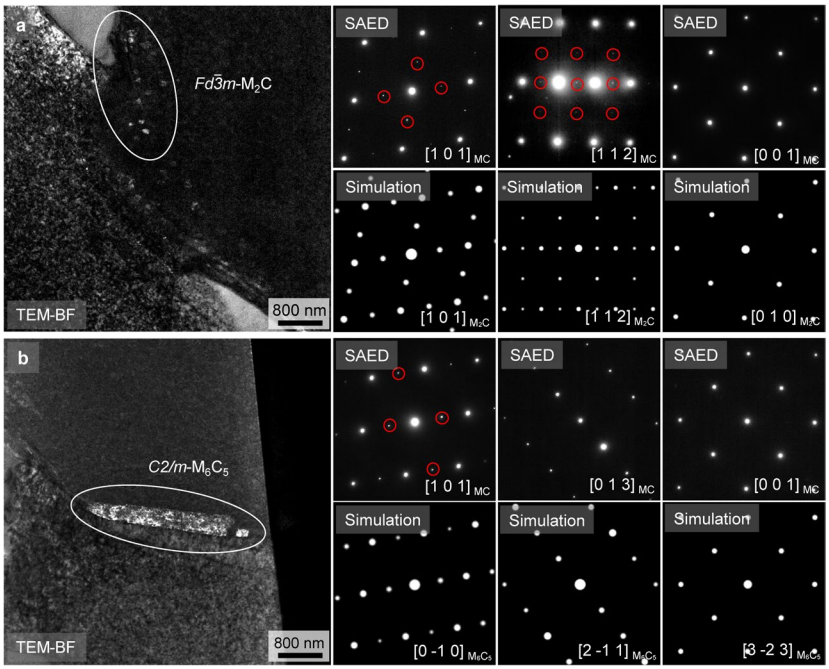

Extended Data Fig. 9 | TEM dark-field (DF) image, experimental and simulated SAED patterns for carbide phases. a, M2C. **b**, M6C5. Experimental SAED patterns were acquired from various zone axes and compared with simulations performed using CrysTBox software. The red circles mark the superlattice diffraction spots corresponding to the DF images.

https://doi.org/10.1038/s41563-026-02680-w

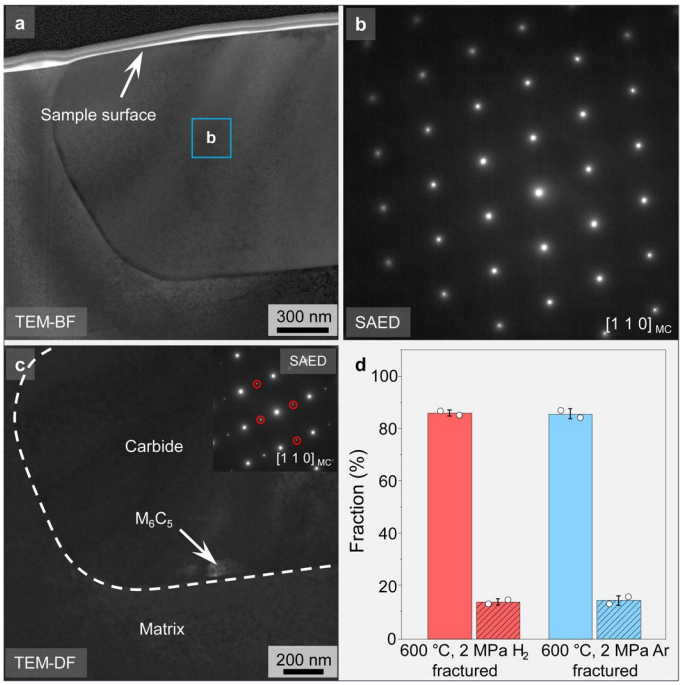

Extended Data Fig. 10 | TEM analysis and statistical characterization of carbide-associated damage after H_2 exposure and deformation at 600 °C. **a**, Overview TEM-BF image taken from the cross-section of a carbide near the sample surface after 2 MPa H_2 charging for ~0.5 h at 600 °C. **b**, SAED pattern acquired from the region indicated by the blue rectangle in **a**. The MC carbide maintains its initial FCC structure with no superlattice structure observed. **c**, TEM-DF image of newly formed carbide. The corresponding SAED pattern shows the distinctive diffraction caused by M_6C_5; the red circles mark the superlattice diffraction spots corresponding to the DF image. No M_2C carbide was identified in the analyzed regions. **d**, Statistical analysis of carbide-associated micro-cracks of specimens deformed under 2 MPa Ar and H_2 at 600 °C. The statistical analysis was performed following the same methodology as that used in Fig. 3b. Data are presented as mean values ± SD. Individual white dots represent independent samples (n = 2 for each condition).